# ROTATIONAL CONTROL WITH PLUME IMPINGEMENT TO AID THE RIGID CAPTURE OF AN UNCOOPERATIVE FAILED SATELLITE

## Giacomo Borelli[*], Gabriella Gaias[†], and Camilla Colombo[‡]

In the framework of Active Debris Removal (ADR) missions employing rigid capture mechanism, the rotational state of the target object greatly influences the feasibility, safety and cost of the capture operations. In this work, the impingement with thruster's plume gases is studied as a strategy to control the target tumbling motion and aid the final approach and robotic operations. The target objects considered in this study are small spacecraft in low Earth orbit, i.e. asset of large constellations, which may require in the future an ADR service solution to ensure the space environment sustainability. A simplified model of the thruster plume is used, and a guidance and control solution is proposed to drive the uncooperative target towards some useful rotational states, defined considering the target geometrical and inertia properties. Simulation results are presented, discussing the feasibility, cost and robustness of the introduced control strategies to increase the collaboration of the failed satellite to be serviced. An additional output is the provision of preliminary guidelines for the grapple fixture location to allow future servicing to an uncooperative failed space assets when a tumbling rate damping phase is required.

## INTRODUCTION

In the last few years, the space sector is experiencing a substantial growth in the number of satellites in the near Earth environment, both already in orbit and planned for launch. A large contribution to this trend is due to the deployment of large constellations for global telecommunication services. The sustainability of the space environment in these conditions will be one of the key challenges of the New Space era. The Inter-Agency Space Debris Coordination Committee (IADC) has proposed mitigation guidelines to reduce the risk of fragmentation events and creation of new debris objects by implementing end-of-life deorbiting strategies, design of demise philosophy and taking protection measures on-board. Nonetheless, it is also foreseen that an active debris removal strategy for at least five large objects in the crowded orbital regions will be required to ensure the stability of the debris environment in the future years.[1–3] An in-orbit demonstration of Active Debris Removal (ADR) technologies, RemoveDebris, was launched in 2018, and more are either planned or under development.[4–6] In this paper, a particular aspect of an ADR mission is studied. Namely, the stabilization of the unknown tumbling motion of the spacecraft to ease rigid capture operations from

[*]Research Fellow, Department of Aerospace Science and Technology, Politecnico di Milano, Via La Masa, 34, 20156 Milano - Italy

[†]Senior Research Fellow, Department of Aerospace Science and Technology, Politecnico di Milano, Via La Masa, 34, 20156 Milano - Italy

[‡]Associate Professor, Department of Aerospace Science and Technology, Politecnico di Milano, Via La Masa, 34, 20156 Milano - Italy

the safety, cost, autonomy and operations complexity points of view. In particular, the focus will be dedicated to small class spacecraft, representative of the assets of mega or large constellations for a future ADR service mission. In this case, the driver for targeting a debris object, other than its large mass, will also be the objects density in its orbital region and the associated risk of collision. This aspect can be of interest for large constellation since they plan to densely populate certain orbital regions to ensure global telecommunication services. In addition, it will be of interest the replacing of the failed asset to ensure nominal constellation coverage of the service to Earth.

A well-known practical difficulty for an ADR mission that uses a rigid capture mechanism is the lack of a precise information and knowledge of the target rotational state prior the actual arrival in the proximity, due to the intrinsic difficulty of measuring it of estimating it from ground observations. Studies and models have been performed on the long term evolution of uncontrolled tumbling satellite motion, which will eventually stabilize into a flat spin about the major axis of inertia thanks to dissipation phenomena.[7] However, the time scale and actual behavior of this dynamics is quite difficult to predict, as it depends on the residual angular momentum after the loss of control of the asset, the energy dissipation mechanisms magnitude, the drag and solar radiation pressure torques and possible collisions with small debris. For example, ESA inoperative spacecraft, ENVISAT, has been observed to have an averaged tumbling rate of 3.5 deg/s, about 20 times faster than the expected estimation from models and simulations.[8,9] For small class assets of large and mega constellations targeted in this paper, the observation and estimation of the debris rotational motion becomes even more difficult due to their reduced characteristic dimensions. To ensure the robustness of a robotic ADR mission, the chaser shall be capable to cope with unknown, fast and random tumbling motion of the debris object to be captured.

One option will be to plan the final approach translational and rotational trajectory of the chaser to synchronize and follow the approach direction of the grapple point of the target. This latter problem is widely addressed in literature for applications such as ADR and On Orbit Servicing (OOS) missions.[10,11] In Ventura et al. an algorithm for on-board sub-optimal generation of approach trajectories to a tumbling target is presented, where the rotational and translational trajectories are obtained through solving a Non Linear Programming (NLP) problem after a parametrization with high-order polynomials the trajectories and applied the inverse dynamics method.[12] Corpino et al. explored both the estimation of the target's state and the 6DOF trajectory planning with Model Predictive Control (MPC) strategy.[13] In Breger and How a method is proposed to include safety in the trajectory optimization of the approach.[14] Artificial Potential Fields (APF) methods are also explored in literature to provide an 6 Degrees Of Freedom (DOF) guidance which prioritize the safety of the trajectory generated.[15,16] Nonetheless, no autonomous capture of an uncooperative and fully non collaborative tumbling object with a rigid mechanism has been performed in space up to now. One of the major complication is the lack of collaboration of the target spacecraft to be serviced, i.e. no active control of the attitude configuration is possible during the close approach and capture/docking operations. This problem is then reflected in complications in the motion planning computational efficiency, autonomy and safety.[17] Efficient and safe methods for approach translational trajectory design to a target with higher level of collaboration, e.g. the collaborative R-bar or V-bar approaches, are widely known from the cooperative rendezvous and docking heritage in the space sector.[18] Another example that simplify 6DOF guidance computation assuming not a complete lack of collaboration is in the work by Hablani et al., where trajectories such as the glidescope approach or the impulsive circular synchronization around the target are developed.[19,20]

The second option to cope with the tumbling rotational motion of the target is to actively control

and modify its rotational state, damping its angular momentum as desired. This strategy is the one targeted in this paper. In this framework, in literature both contact and contactless methods have been analyzed. Contact methods, with technologies such as a contact tip or a robotic flexible brush have been studied.[21,22] Though this methods could be cheap and effective, the danger of generating new debris with the contact forces on a spacecraft of unknown conditions will represent a major drawback for their applications in actual in orbit operations. On the other hand, contactless methods of acting on the target debris rotational motion are of great interest, despite the Guidance Navigation & Control (GNC) complications and complexity. The safety associated to these strategies is much higher, and is ensured by the fact that the chaser can perform the control actions from a predefined safe distance from the target. Example of contactless technologies explored in literature are electrostatic, magnetic interactions, and laser ablation.[23–26] Another strategy, of interest for this paper, uses exhaust gasses from the chaser on-board thrusters to obtain the control action on the target rotational state. This method has been explored in literature for upper stage rocket bodies and the ESA ENVISAT inactive satellite.[27–30] Its advantages can be mainly summarized in: higher control action with respect to other contactless method, safe operations distant from the target, and the availability of the payload/systems to perform the operations already on-board the chaser. In this paper, the control capabilities of the plume impingement strategy is explored, focusing on the control of the target towards different rotational states, particularly defined to increase its level of collaboration in close proximity. The contributions of this paper are to evaluate the feasibility and cost of this strategy, together with with identifying limitations from the control aspects of the impingement method. In addition, supported by obtained paper results, preliminary guidelines about the grapple fixture location for large constellation assets to comply with plume impingement and safe capture operations are discussed.

The paper is organized as follows: At first, the force model used for the the plume impingement mechanism is described, together with the impingement operations dynamics and system geometry. Subsequently, different control scenarios, e.g control objective, are introduced by considering rotational stable end condition of the target debris to allow easier and safer approach trajectories and capture operations. After the critical analysis of the results, conclusions about the control behavior are drawn.

## MODEL DESCRIPTION

### Plume force model

The contactless strategy of stabilizing the tumbling motion of the target debris object with plume impingement relies on the action of the plume gasses of the chaser thrusters onto the target's surfaces. As previously stated, no additional payloads or systems on the chaser are required for this particular proximity phase other than the thrusters already available on-board. The model used here for the plume interaction is the analytical model by Fehse.[31,32] In this model, the pressure field inside the gas exhaust plume is modeled as follows:

$$P(r,\theta) = Ce^{-\frac{\theta^2}{2\theta_0^2}}r^{-2} \tag{1}$$

where $r$ and $\theta$ are respectively the distance of the point with respect to a reference frame centered at the thruster exit nozzle and the angle between the Line Of Sight (LOS) of the nozzle exit and the point. The half cone angle $\theta_0$ represents the $1\sigma$ value of thruster plume width. The thrust constant

3

$C$ is evaluated using continuity consideration on the flow with Equation (2):

$$C = \frac{F_0}{\pi \int_0^\pi e^{-\frac{\theta^2}{2\theta_0^2}} \sin(2\theta)d\theta} \tag{2}$$

where $F_0$ represents the thrust level of the chaser thruster creating the impingement plume. Alternative and more accurate models are studied in literature to describe the plume gas dynamics, such as the Simons analytic model, which better represent the boundary layers in the plume, or the CFD high fidelity simulations.[27,29] However, the focus of this work has been on evaluating the properties and performances of the control system and strategy and its dependency to the target shape, inertia, and target impingement motion; the refinement of the force model will be addressed in future works. The gas impinging the target's surface is assumed to be in free molecular regime, and the interaction force described by the following equation:[30]

$$d\mathbf{F} = -P(r,\theta)\cos\gamma\left[(1-c_s)\hat{\mathbf{S}} + 2\left(c_s\cos\gamma + \frac{1}{3}c_d\right)\hat{\mathbf{N}}\right]dS \tag{3}$$

where the the flow is reflected in a diffuse and specular fashion by the surface according to the respective coefficient $c_d$ and $c_s$.[30] The angle $\gamma$ is the angle between the surface normal, $\hat{N}$ and the thruster Line Of Sight (LOS) $\hat{S}$, while the impinged surface area is denoted as $dS$. Specific values of the parameters describing the diffuse reflection can be consulted in Table 1, where also the other main parameters of the plume models are reported.

**Table 1**: Chaser thruster and plume parameters.

| $I_{sp}$ [s] | $F_0$ [N] | $\theta_0$ [deg] | $c_s$ [-] | $c_d$ [-] |
|---|---|---|---|---|
| 285 | 10 | 12 | 0.03 | 0.97 |

**Targets geometry**

Two different geometries of small class spacecraft have been studied. The inertia and geometry characteristics for the two representative models are reported in Table 2. The Target Body Frame (TBF), for both targets, is defined at the spacecraft Center of Mass (CoM), located at the center of the cubic spacecraft body, and is assumed to be aligned with the principal axis of inertia. Figure 1 depicts the pressure distribution over the target 1 surfaces as a result of the plume model used, with the parameters of Table 1.
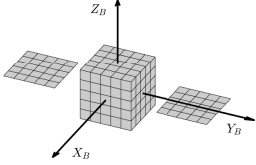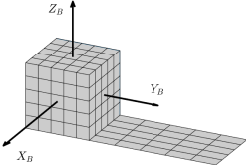
**System geometry and dynamics**

During the plume impingement phase the chaser and target spacecraft are considered orbiting in a circular orbit with 1200 km of altitude and 87.9 deg of inclination. The proximity operations are modeled in the Radial-Tangential-Normal reference frame centered on the target's Center of Mass (CoM). The target rotational dynamics are described using Euler equations and the kinematics expressed in quaternion formulation:[33]

$$J\dot{\boldsymbol{\omega}} = J\boldsymbol{\omega} \times \boldsymbol{\omega} + \mathbf{T}_{gg} + \mathbf{T}_c \tag{4}$$

$$\dot{q}(t) = \frac{1}{2}\Omega(\boldsymbol{\omega})q(t) \tag{5}$$

**Table 2**: Target spacecraft models geometry and inertia properties.

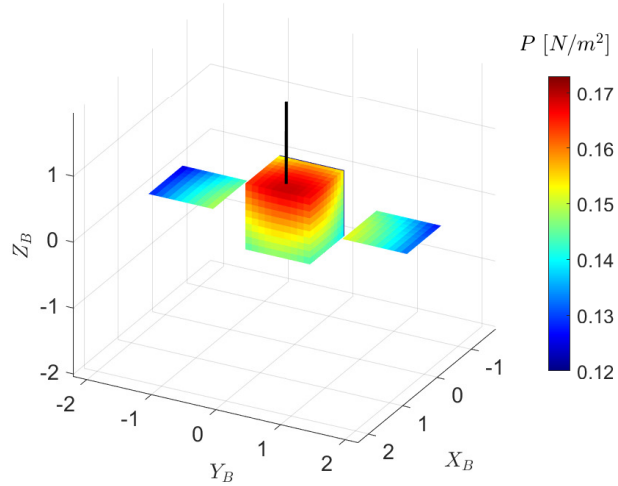| | | | |
|---|---|---|---|
| **TARGET 1** |  | $J_{xx} = 40 \ \mathrm{kg\,m^2}$    **Body**: $1 \times 1 \times 1$ m | |
| | | $J_{yy} = 25 \ \mathrm{kg\,m^2}$    **Panels**: $1 \times 1$ m | |
| | | $J_{zz} = 50 \ \mathrm{kg\,m^2}$    **Panel center**: $[0, \pm1.5, 0]$ m (TBF) | |
| **TARGET 2** |  | $J_{xx} = 45 \ \mathrm{kg\,m^2}$    **Body**: $1 \times 1 \times 1$ m | |
| | | $J_{yy} = 25 \ \mathrm{kg\,m^2}$    **Panel**: $1 \times 2$ m | |
| | | $J_{zz} = 50 \ \mathrm{kg\,m^2}$    **Panel center**: $[0, 1.5, -0.5]$ m (TBF) | |



**Figure 1**: Pressure distribution on the target 1 surfaces facing the thruster plume. The thruster nozzle exit is at 16 m of distance from the target CoM.

$$\Omega(\omega) = \begin{bmatrix} 0 & \omega_z & -\omega_y & \omega_x \\ -\omega_z & 0 & \omega_x & \omega_y \\ \omega_y & -\omega_x & 0 & \omega_z \\ -\omega_x & -\omega_y & -\omega_z & 0 \end{bmatrix} \tag{6}$$

In Equation 4, $\boldsymbol{\omega}$ is the target angular velocity vector in the body frame, and $J$ the inertia matrix, considered diagonal for the target models introduced. Together with the impingement control torque $T_c$ acting on the target rotational dynamics, the gravity gradient disturbance $T_{gg}$ is also considered.

During the impingement operations the chaser is assumed fixed at a +T hold point. Such formation was selected for two main reasons. First, it is a favorable stable position according to the linearized relative motion dynamics. Then, the impingement force on the target will produce a braking force opposite to the target velocity that will contribute the orbit lowering, hence the deorbiting

of the target. In this study, the relative motion control and station keeping is not implemented, and is assumed to be perfectly performed by the chaser platform.

The last two fundamental assumptions made on the system are the perfect chaser attitude control during the impingement operations and the availability of the pose estimation solution of the target. These assumptions can be dropped including more complete and realistic simulation scenarios. However, the system and models have been simplified to better assess the plume impingement control capabilities and cost in increasing the collaboration of small targets with different geometries.

**Impingement Guidance and Control Algorithm**

The algorithm to control the target rotational motion is based on the planning of the pointing of the on-board thruster towards the target's surfaces. The forces exerted to the target surfaces are highly dependent on the thruster LOS and surface orientations with respect to the chaser. As expected, this characteristic greatly reduce the control authority of the plume impingement strategy in controlling the target's rotational state. The geometry of the system and impingement operations is displayed in the target RTN frame in Figure 2, where $r_{LOS}$ represents the thruster center line LOS, $r$ the distance from the target surface with respect to the thruster nozzle exit and $n_s$ the normal to the surface element $\mathrm{d}S$.
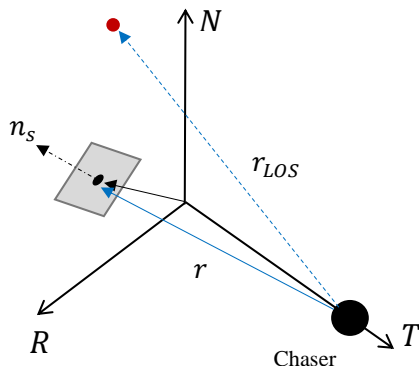


**Figure 2**: Impingement control problem geometry.

To decide the impingement control objective, a guidance torque law $\mathbf{T}_{des}$ is introduced. In this study, different guidance laws have been tested, based on simple feedback dependent on the state estimation solution, and will be discussed in depth in the next section.

The control algorithm decides the pointing and firing of the thruster towards the target using a simple logic. $N_t$ candidates points are defined on the target's surfaces and the resultant torque effect for each of this pointing solution is evaluated with the force model. The decision of whether to fire or not the thruster and towards which candidate point is mainly structured in two layers. At first, the direction of the torque obtained for the different candidate points $\mathbf{T}_{c-i}$ is compared to the

guidance torque vector $\mathbf{T}_{des}$ direction. At this point, only the $N_t$ that are below a certain threshold of direction error, evaluated with Equation (7), are retained.

$$\delta = \frac{\mathbf{T}_{des} \cdot \mathbf{T}_c}{T_{des} \cdot T_c} < \epsilon \qquad (7)$$

If no candidates points fulfill this condition, the chaser simply does not fire the thruster. The value of the angle tolerance $\epsilon$ is taken between 10 and 60 degrees, according to peculiar geometrical properties of the target. In general, increasing the threshold $\epsilon$ the impingement control is bound to follow the guidance torque less accurately, resulting in a coarser control. Usually, the effect is to produce spurius torques with respect to the desired ones and to increase the firings needed fulfill the control objective. But this expected behavior, is not always observed due to the non linearity of the attitude dynamics and on the complicated impingement control properties. In the second layer, the retained candidate points are selected considering the torque magnitude, simply evaluating the ratio of desired and obtained torque with Equation (8) and bounding it between an upper and lower bound values.

$$D_i = \frac{T_c}{T_{des}} \qquad (8)$$

The lower and upper bounds of $D_i$ are taken respectively as 0.01 and 4. If then more than one candidate points satisfy these two layers of checks, the one with the higher $D_i$ is selected.

The other main feature of the impingement control algorithm is its operation and control flow in the simulation. The impingement algorithm which decides the thruster pointing it is in fact run at a certain sample time $\Delta T_s$ in the simulations. In details, the control flow is managed as follows. The chaser gets the measurement and estimation of the pose at time $t_{i-1}$. The target state is then propagated for the sample time $\Delta T_s$, and the pointing algorithm is evaluated considering the target state at $t_i = t_{i-1} + \Delta T_s$. Once the required pointing of the thruster at $t_i$ is obtained, the thruster is then fired starting at $t_i$ for $\Delta T_t$. The thrusting time is modulated according to the value $D$ of Equation (8), and the maximum threshold is set to 5 seconds. The control flow logic in time is displayed in Figure 3. The value of the sample and thrusting time are reported in Table 3. It can be noted how the algorithm sample time is taken quite large. This assumption, and the rationale on introducing such control logic and flow, is mainly motivated by the operability requirement of the algorithm and plume impingement strategy. In fact, it is considered that during the control sample time windows, the chaser has the time to perform the data acquisition with the sensors, the pose estimation, the attitude maneuvers to achieve the pointing required at $t_i$ and other operations, i.e. telemetry download.
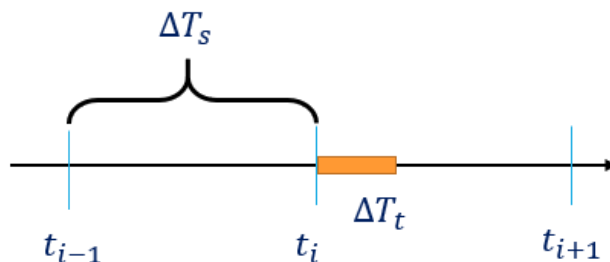


**Figure 3**: Control flow logic in time.

**Table 3**: Impingement pointing algorithm parameters.

| $\Delta T_s$ [s] | $\Delta T_{t-max}$ [s] | $r$ [m] |
|:---:|:---:|:---:|
| 30 | 5 | 16 |

In Table 4, the computational performance of the on-board algorithm for the impingement operations are reported, comprehending the state propagation of the pose estimation solution at $t_{i-1}$ and the pointing algorithm logic considering $N_t = 54$ candidate points on target 1. The different values are obtained refining the mesh discretization step $N_s$ of the target surfaces. Propagation of the target rotational state is done using a multi-step Adams-Bashford-Moulton scheme.

**Table 4**: Impingement pointing algorithm computational performances.

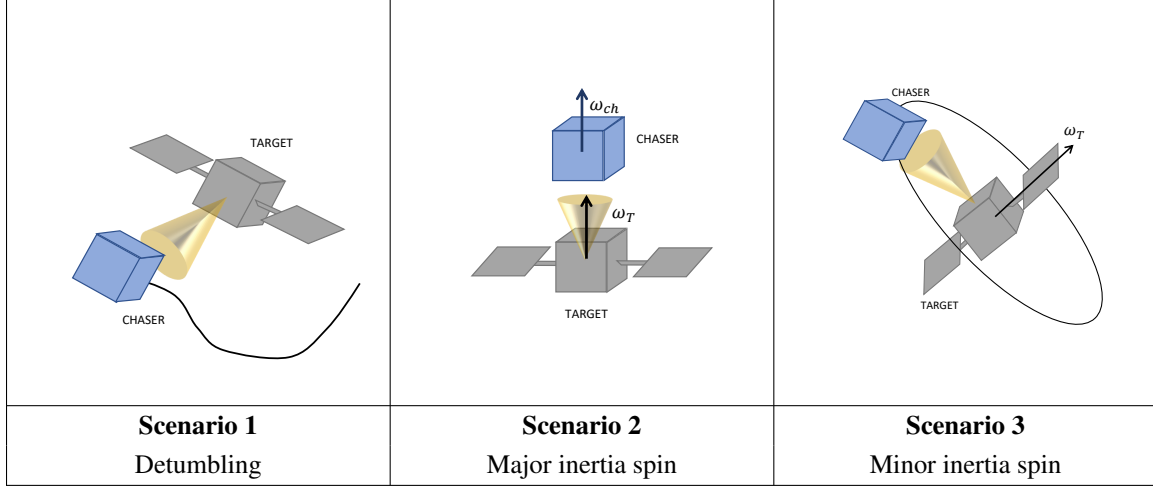| $N_s$ | 5 | 10 | 20 |
|:---:|:---:|:---:|:---:|
| $T_{CPU}$ [s] * | 0.1112 | 0.1128 | 0.2328 |

## CONTROL SCENARIOS

According to the different objectives of the impingement control, different guidance torque laws are introduced. The rationale on selecting the control scenarios to be simulated is motivated mainly by the stability of the motion after the impingement control switch off. In fact, a stable attitude motion will greatly aid the final approach trajectory control and the robotic arm and manipulator control to capture the target. The stability will create an artificial collaboration characteristic of the initially non-collaborative satellite, giving it a prescribed attitude motion that is maintained in a stable manner. During fast tumbling motion, the trajectory generation, both for the final approach and manipulator operations, results in a more complex 6 DOF guidance problem, difficult to be autonomously managed on-board. In addition, the safety requirement could be quite stringent and result in unfeasible capture for spacecraft with relevant tumbling motion and large moving appendages. The three main scenarios introduced are: (1) detumbling of the target rotational motion, (2) spin generation along the target major axis of inertia, and (3) spin generation along the minor axis of inertia. In all these cases, the target will then maintain the motion in the time span between the end of the impingement phase and the Go command for final approach and capture operations. Depending upon the targets' geometries, the latter operations will have a certain complexity and cost. In Table 4 is shown the scheme of the approach and capture operations for the different scenarios introduced, with illustrations of the final operations scheme taking as an example target 1. The gold cone represents the approach corridor to be exploited by the chaser to perform capture/docking with the target.

For the three different scenarios, the approach corridor exploited by the chaser and the manipulator/robotic arm operations and work-space are influenced by the target rotational motion. In scenario 1, the target is controlled damping all the residual angular rates below a prescribed threshold. Here the target can be approached in either one of the body axes since the tumbling motion is brought to an almost stationary state. Thus, the approach corridor will be defined considering the the actual geometry, appendages location and the grapple fixture on the target. The guidance law used for the

---

*The run time reported is obtained using an Intel(R) Core(TM) i7-5500U @2.40GHz with the MATLAB® algorithm implementation.

**Figure 4**: Control scenarios introduced for the guidance law used in the impingement control.



| Scenario 1 | Scenario 2 | Scenario 3 |
|:---:|:---:|:---:|
| Detumbling | Major inertia spin | Minor inertia spin |

detumbling scenario is a simple proportional control against the target's angular momentum vector $\mathbf{h}_L$ expressed in the RTN frame.

$$\mathbf{T}_{des} = -K\mathbf{h}_L \tag{9}$$

In scenario 2 the target is controlled towards a major axis spin, and within this control scenario two different guidance laws are tested. The first one generates the major axis spin and redirects it towards a fixed inertial direction. While, the second one simply generates the required spin damping the residual angular rates in the other axis of the TBF. In both cases, since inside the plane perpendicular to the major axis of inertia large appendages and mass are usually located, the safe approach corridor simply reduces to the direction of the target angular momentum, hence the major spin axis direction. Capture operations can then be carried out simply synchronizing chaser attitude motion to the target spin without acting on the translational synchronization control. For both cases the approach and capture operations become more similar to the collaborative and cooperative approaches, thanks to the fixed inertial direction of the spin axis. The first one will even increment further the collaboration of the target by controlling also the direction of the spin axis, and driving it towards peculiar directions in the RTN frame useful for the approach operations. For example, in this study, the selected direction is the N unit vector of the RTN reference frame, which will be, such that the spin axis will have constant direction even in the RTN frame, perspective of the chaser. In the first case the guidance law is obtained using a quaternion tracking law to a moving frame, which shows the spin motion directed in the desired direction.[33]

$$\mathbf{T}_{des} = -K_1\boldsymbol{\omega}_{BL'} - K_2\delta\mathbf{q} \tag{10}$$

where $\boldsymbol{\omega}_{BL'}$ is the angular velocity error of the body with respect to the reference moving frame $L'$, $\delta\mathbf{q}$ the configuration error of the target expressed as a quaternion error, and $K_1$ and $K_2$ the control gains of the two proportional terms. On the other hand for the second case a simple proportional law dependent on the error between the target body angular rate a reference body spin is used.

$$\mathbf{T}_{des} = -K\big(\boldsymbol{\omega}_{BN} - \boldsymbol{\omega}_{BN,ref}\big) \tag{11}$$

The guidance laws selected are trivial and simple proportional laws which in principle do not ensure the stability of the target control with plume impingement. However, the impingement control

has a very reduced control authority that depend on the target surface orientation. The pointing algorithm to ensure propellant efficiency and avoid unnecessary firings with limited torque effect, and the sample time of the control driven by operative constraints, will result into a control action of impulsive characteristic which will be less or not at all accurate in following complex guidance laws based on the continuous state errors.

The scenario 3 consist in generating the minor inertia axis spin in the target motion. As for scenario 2, also here two different control cases are explored, one which controls also the kinematics of the target's motions redirecting its spin towards a certain inertial direction; while the other one that generate the minor axis spin only in the target body frame, controlling only the target's dynamics in TBF. The guidance laws fed to the impingement pointing algorithm are the same introduced in Equation (10) and (11) for scenario 2. The approach corridor for this control scenario will most likely be perpendicular to the spin axis, being the minor axis of inertia the one along which are distributed the large appendages. In this case to approach the target, a synchronization of the translational motion of the chaser with the spin motion of the target is needed. Nonetheless, these type of translational synchronization will be easier thanks to the stable and regular spin motion of the target. An additional advantage will be that the large appendages of the target, usually spread along the minor axis of inertia, will span a much limited space around the target, increasing the safety of operations and decreasing the collision risks.

In summary, the control and simplification of the target rotational motion through the introduction of this control scenarios has the objective of increasing safety and decrease trajectory (final approach and robotic arm) computational complexity. This two latter features will strongly contribute to the possibility of performing the approach and capture proximity operations in an autonomous fashion.
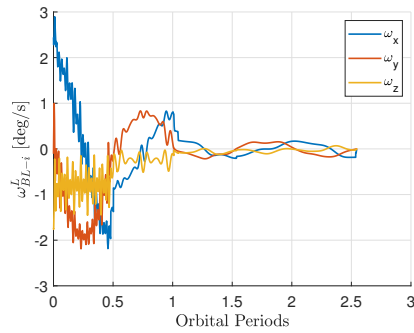
## SIMULATION RESULTS

In this section the simulation results for the control scenarios are presented for the two different small spacecraft models defined in the previous section. In the three control scenarios, four different initial conditions of angular rates are considered, encompassing the cases where the target's angular momentum is initially distributed along the 3 different axis of the TBF. Magnitude of the initial angular rate conditions is selected to be approximately 3 deg/s. For each angular rate initial condition, 64 simulations are performed with different initial attitude configuration of the target with respect to the chaser. The models and control scenarios are developed and simulated in MATLAB$^{®}$ & Simulink environment, with a Runge-Kutta scheme with maximum time step of 0.2 seconds.
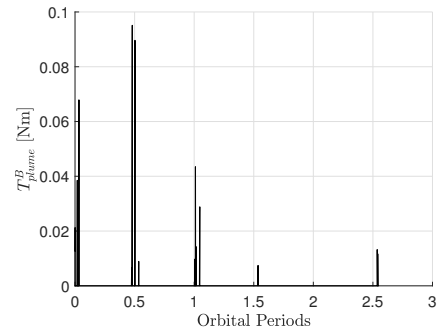
### Scenario 1: Detumbling

The simulation results for the detumbling control scenario are reported in the followings. The threshold to stop the simulation and consider the detumbling control successful is the damping of the target's angular velocity magnitude below 0.05 deg/s.

In Figure 5 the angular rate of the target in the RTN frame (left) and the magnitude of the resulting torque on the target (right) for a single simulation of detumbling control performed to target 1 are shown. On the left, $\omega_{BL-i}^L$, represents the components of the angular velocity of the body frame (B) with respect to the RTN frame (L), expressed in RTN frame (denoted with the superscript L). In Figure 6 the results for the multiple simulations performed for the initial angular rate $\boldsymbol{\omega} = [\sqrt{3}, \sqrt{3}, \sqrt{3}]$ deg/s with different initial attitude configurations both for target 1 and target 2 are displayed. On the left side the evolution of the magnitude of the target angular rates are shown

with respect to the RTN frame for the 64 different simulations, while on the right the distributions of the propellant spent by the impingement thruster for the multiple simulations with different initial relative attitude configurations.
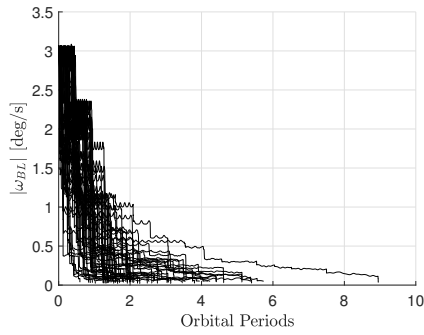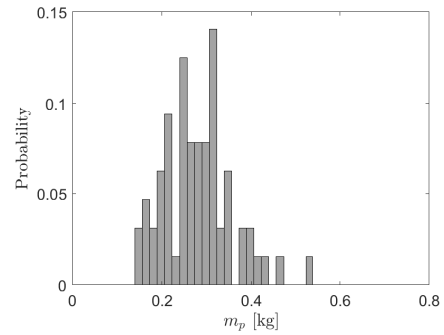


(a) Angular rates with respect to RTN frame.



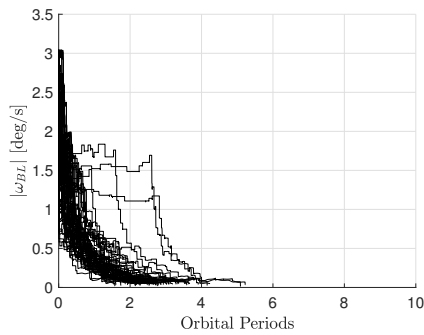(b) Resulting control torque magnitude on the target.

**Figure 5**: Results for a single simulation for the detumbling scenario of target 1, considering as initial condition $\boldsymbol{\omega}_0 = [\sqrt{3}, \sqrt{3}, \sqrt{3}]$ deg/s.
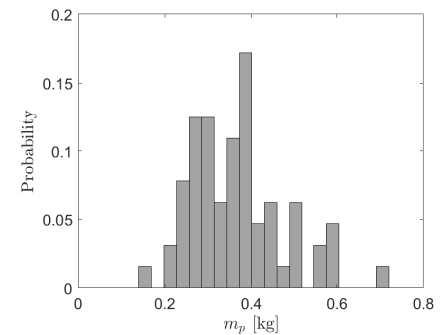


(a) Target angular rates magnitudes.



(b) Propellant mass cost distribution.



(c) Target angular rates magnitudes.



(d) Propellant mass cost distribution.

**Figure 6**: Results for the 64 different simulations of initial angular rate $\boldsymbol{\omega}_0 = [\sqrt{3}, \sqrt{3}, \sqrt{3}]$ deg/s scenario 1 control performed to target 1 (a) and (b) and target 2 (c) and (d).

11

It can be immediately appreciated how the detumbling control has quite different behavior depending on the initial target configuration, with propellant cost that in some cases be double with respect to other some advantageous initial configurations, due to the high dependence of the control actions to the target surfaces orientations and facing. The impingement control to fully damp the target angular momentum for both targets is in the same order of propellant cost, however, for the second spacecraft the propellant used is noticeably more distributed towards higher values.

In Table 5 are shown the results for the whole set of initial angular rate conditions, reporting the mean $\overline{m}_p$, standard deviation $\sigma_{m_p}$, and the maximum value of the propellant consumption for the different initial attitude configurations simulations. The propellant mass cost reported is the only the one consumed by the impingement thruster. During operations, other propellant expenses will be present, i.e. chaser station keeping to maintain the hold point, attitude control to perform pointing and if necessary target observation, and cosine losses of the thrusters configurations. This contributions will depend on different aspects. For example, the attitude control will depend on the chaser-target distance which will influence the width of the cone to be covered in order to point to the target surfaces. The closer the chaser is to the target, the larger the attitude pointing maneuvers for the impingement algorithm will result. On the other hand, the cosine losses will depend on the chaser thruster configurations. Station keeping cost can be more directly estimated in at least the same cost used for impingement, since the chaser at each impingement firing towards the target will need to fire in the same way another thruster in the opposite direction to prevent drifting from the target.

**Table 5**: Scenario 1 simulations results for the two target geometries considered.

| | $\overline{m}_p\ [kg]$ | | $\sigma_{m_p}\ [kg]$ | | $\max(m_p)\ [kg]$ | |
| --- | --- | --- | --- | --- | --- | --- |
| $\omega_0$ [deg/s] | S/C 1 ($N_f$) | S/C 2 ($N_f$) | S/C 1 | S/C 2 | S/C 1 | S/C 2 |
| $[\sqrt{3}, \sqrt{3}, \sqrt{3}]$ | 0.281 | 0.367 | 0.077 | 0.109 | 0.536 | 0.705 |
| $[3, 0.1, 0.1]$ | 0.337 | 0.452 | 0.117 | 0.251 | 0.680 | 1.657 |
| $[0.1, 3, 0.1]$ | 1.385 | 0.607 (6) | 0.086 | 0.307 | 1.644 | 2.132 |
| $[0.1, 0.1, 3]$ | 0.477 | 0.372 | 0.121 | 0.110 | 0.797 | 0.743 |

The impingement algorithm parameters are tuned differently for the peculiar simulations cases, both in terms of direction error limit $\epsilon$ and in terms of control gains introduced in the guidance laws. The control gains $K_i$ in the proportional guidance laws are tuned such that for each case, the desired torque magnitude $T_{des}$ is about the same order with respect to the torque achievable by the impingement plume by pointing in a advantageous direction, i.e. panels of the target model. While the direction error $\epsilon$, for example in the detumbling of target 1, will constrain the impingement torque $T_c$ to be within a 10 degrees cone around the guidance torque $T_{des}$ for all the initial condition except the one with initial angular rate along the Y axis of TBF, where the $\epsilon$ is taken as 30 deg. This represents a quite stringent requirement to ensure an high propellant efficiency avoiding spurious control torque components of the impingement effect. On the contrary, the simulations with such stringent condition on the guidance torque matching for target 2 do not provide the desired control action, so the $\epsilon$ angle is increased to 60 deg for all the simulations. This behavior is associated to the geometry of target 2, which features the side panel in a position in TBF in which any impingement action towards that panel will eventually produce torque in every direction, being surface located
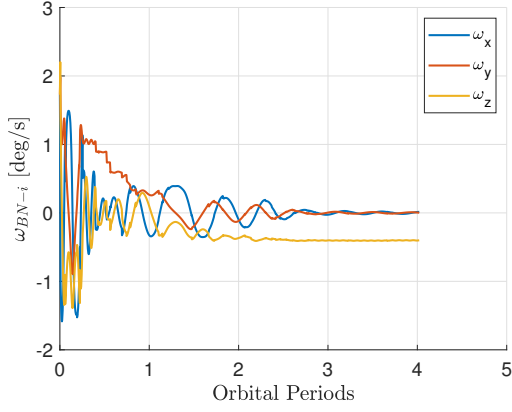
below the CoM TBF location. An higher $\epsilon$ will in general result in a much less accurate control that will reflect in the lower efficiency of performing the detumbling as dictated by the guidance law. Exception to this behavior are the simulation batches correspondent to initial angular rate along the Y and Z body axis. In both case, the longer panel of target 2 gives control authority in these two TBF axis, thanks to the larger surface and distance to the CoM with respect to the panels of target 1. In the first two cases, the tumbling motion will in general redistribute the angular rate with the torque free motion between the impingement control firing, giving much more perspective from the chaser LOS to the target's surfaces, thus the poor accuracy of the control in obtaining with precision the guidance torque reflects in worse performances of target 2 control with respect to target 1. For the simulation cases for target 2 where the initial angular rate is mostly along the Y axis, there are some initial attitude configurations of the target that either do not trigger any firings or unstabilize the spacecraft instead of reducing its angular momentum. In particular, the number of failed control simulations is denoted with $N_f$ in Table 5. This failures are mainly caused by the reduce control authority in generating a torque along the Y axis of the TBF of target 2 for its slim geometry. And in addition, to the fact increasing the $\epsilon$ to account for the panel displacement and asymmetry with respect to the center of mass, results in a less accurate guidance, which can some times fail to decrease the target angular momentum and instead increase it, being the control provided in open-loop based on the evaluation at $t_i$.
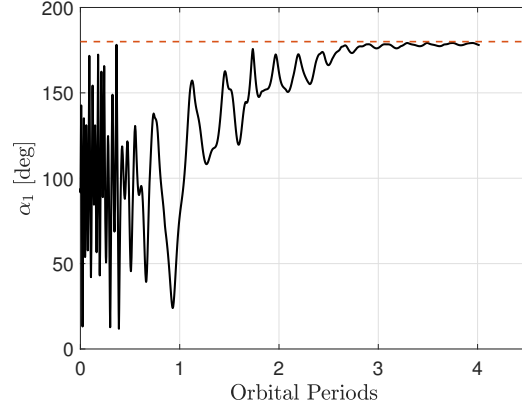
**Scenario 2: Major inertia spin**

In this section the major inertia spin scenario results are reported, for both the control cases in which the major axis spin is redirected towards a constant direction or simply generated in the TBF. The guidance laws for the latter cases are respectively reported in Equation (10) and (11). In both cases, the magnitude of the desired major inertia spin motion is set to 0.4 deg/s. In the spin redirection control, the target's spin is redirected towards the N direction of the RTN frame, which remains inertially fixed considering a Keplerian motion. This direction is arbitrary, a fixed direction lying in the orbital plane could have been selected to allow the R-bar or V-bar approach in the orbit location when, along the orbit, the spin axis will coincide with either of these axes thanks to the RTN motion. The simulations for this scenario are stopped when the magnitude of the desired torque falls below a threshold, which is set to allow direction errors in the spin axis direction (in the spin redirection control) of about 5 degrees, and errors of about 0.05 deg/s for the desired angular rates. In Figure 7 the results for a representative simulation of scenario 2 control applied to target 2 are shown. On the left are displayed the body angular rates, where it can be appreciated how the Z body spin is successfully generated. While on the right is shown the time history of the angle $\alpha_1$ between the spin axis and the N direction, successfully drawn to the 180 degree value corresponding to a direction parallel to the N unit vector. On the other hand, in Figure 8 a representative simulation of the major inertia axis body spin generation control for target 2 is shown, where it can be noted how the angle between the the spin axis and N direction is not drawn to the either 0 or 180 deg value, Figure 8(b), while the Z spin is generated in the TBF frame, Figure 8(a).

In Table 6 the complete results for all initial conditions simulated in scenario 2 for both spacecraft models are reported.

The cost of spin redirection, is in general higher than the spin control in the TBF and also the detumbling scenario. However, for target 2, in the case when the initial angular rate of the target is either mostly along the Z axis TBF or in a tumbling state (first and second row of the Table 6), the cost is comparable or slightly less than the scenario 1 simulations with the same initial conditions.
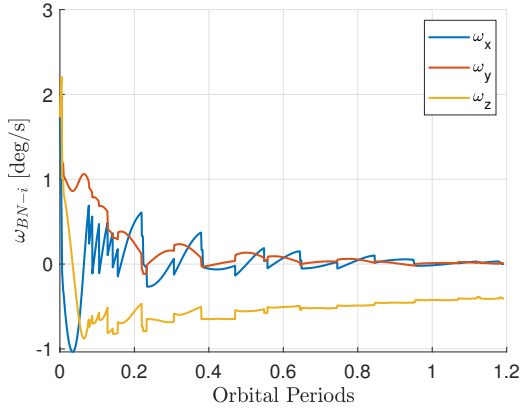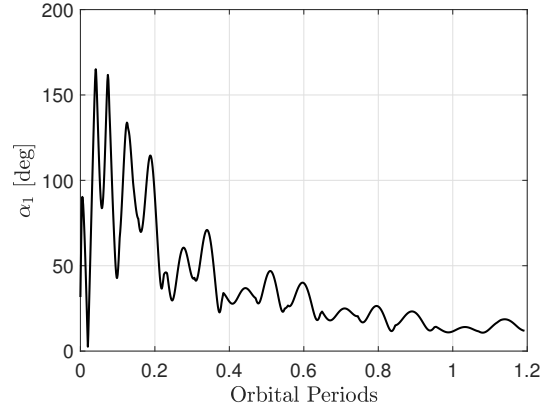
(a) Target body angular rates.

(b) Spin axis angle with respect to N.

**Figure 7**: Results for a representative simulation of scenario 2 (spin redirection control) for target 2 with initial angular rate equal to $\omega_0 = [\sqrt{3}, \sqrt{3}, \sqrt{3}]$ deg/s.



(a) Target body angular rates.

(b) Spin axis angle with respect to N.

**Figure 8**: Results for a representative simulation of scenario 2 (body spin control) for target 2 with initial angular rate equal to $\omega_0 = [\sqrt{3}, \sqrt{3}, \sqrt{3}]$ deg/s.

Here the impingement control has good control authority along the Z axis thanks to the large side panel, and allows an efficient control in both generating the spin in TBF, and redirecting it along an N inertially fixed direction. In addition, the residual angular momentum left along the spin axis contributes positively to the propellant saving with respect to scenario 1. As for scenario 1, the $\epsilon$ value for target 2 is increased to 30-60 deg value to account for the geometrical complications of having stringent constrain logic in the pointing algorithm. Simulations for target 2 where the initial angular rate is mostly along the minor axis of inertia (Y TBF) show quite a relevant number of failures in achieving the the control objective, either because the impingement is not initially triggered or because, within the firing time, the impingement torque effect evolves to a de-stabilizing effect on the angular rates. The latter cause is mainly due to the open loop nature of the control algorithm, that evaluates the pointing at $t_i$ and maintains throughout the firing time, as the target

14

**Table 6**: Scenario 2 simulations results for the two target models considered.

| | $\omega_0$ [deg/s] | $\overline{m}_p$ [kg] | | $\sigma_{mp}$ [kg] | | $\max(m_p)$ [kg] | |
|---|---|---|---|---|---|---|---|
| | | S/C 1 ($N_f$) | S/C 2 ($N_f$) | S/C 1 | S/C 2 | S/C 1 | S/C 2 |
| RTN Spin | $[\sqrt{3}, \sqrt{3}, \sqrt{3}]$ | 0.554 (2) | 0.438 | 0.093 | 0.071 | 0.811 | 0.588 |
| | $[3, 0.1, 0.1]$ | 0.565 (1) | 0.396 | 0.082 | 0.090 | 0.830 | 0.611 |
| | $[0.1, 3, 0.1]$ | 1.621 (1) | 0.753 (12) | 0.084 | 0.286 | 1.872 | 1.689 |
| | $[0.1, 0.1, 3]$ | 1.187 (1) | 0.334 | 0.145 | 0.097 | 1.497 | 0.564 |
| Body spin | $[\sqrt{3}, \sqrt{3}, \sqrt{3}]$ | 0.339 | 0.193 | 0.052 | 0.092 | 0.462 | 0.817 |
| | $[3, 0.1, 0.1]$ | 0.339 | 0.169 (9) | 0.070 | 0.096 | 0.570 | 0.743 |
| | $[0.1, 3, 0.1]$ | 1.530 | 0.412 | 0.119 | 0.120 | 1.931 | 0.798 |
| | $[0.1, 0.1, 3]$ | 0.428 | 0.1364 | 0.106 | 0.0389 | 0.758 | 0.2639 |

rotates. Instead, in target 1 simulations only few failed attempts are observed in the spin redirection control. In this cases, rather than lack of initial triggering of firing or the unwanted impingement effects due to target's rotation, the failed simulations are characterized by an end condition that shows a minor axis body spin instead of a major axis spin directed towards the N direction. This peculiar behavior, is associated with the ability of the impingement control to better correct the dynamic part of the guidance law of Equation (10), rather than the kinematic part. Hence, the target angular velocity is driven to the N direction, but it is generated a minor axis instead of a minor axis spin. This behavior is observed in a very limited number of simulations despite being applicable to all simulation cases, mainly because the control authority in creating the torque along the major axis direction is much higher than the one characteristic of the minor axis. Therefore, the control is almost always drawn to follow that condition and generate a major axis spin in TBF directed towards the N direction, rather than the minor axis. This property is discussed and explained further in the next section where the results of scenario 3 are presented.

**Scenario 3: Minor inertia spin**

The last simulation results presented are the one associated to scenario 3, where the same control objectives of scenario 2 are defined but instead considering the generation and redirection of a minor inertia axis spin on the target. In the spin redirection control case, the peculiar behavior observed in only a small subset of simulations of scenario 2 becomes more evident. In particular, for both target 1 and target 2, the impingement control to generate and redirect the minor axis spin motion is not effective, and the simulations show instead the generation and redirection of a Z spin towards the N fixed direction, as shown in one simulation in Figure 9. This behavior is associated to the fact that target 1 and target 2 geometries allow very little control authority in the minor inertia axis, e.g. Y axis of TBF for the slim shape of the objects. In addition, the open loop nature of the control acting with almost impulsive actions on the target rotational motion, results in a control that is effective in controlling the dynamics of the target, but much less adapt to drive the kinematics error to zero. Looking at Equation (10), the first proportional term dependent on the angular rate error dominates the control as the impingement strategy controls the target angular velocity towards the N direction. However, the kinematics error reduction is not successfully enforced by the thruster firings upon the

target, leading the motion to evolve towards a Z major axis spin, characterized by higher control authority. In summary, the control on the kinematics of the target is proven to be ineffective with the impingement strategy introduced. Moreover, simulations where the weight of the kinematic error term (quaternion error with respect to the desired one) is increased, show an unstable behavior where the control never achieve any stable condition and the firings are not able to drive the target dynamics to the guidance law evolution properly. This behavior, is associated to the fact that the kinematic error has in general an higher frequency of variation rather than the error in the angular rate, and the impingement control is not able to manage and control it. As for scenario 2, some particular simulations may succeed to have a Y body spin successfully redirected towards N, simply thanks to the advantageous initial conditions and evolution of relative configuration of the target with respect to the chaser. In the cases, where targets 1 and 2 are initially tumbling this behavior is not seen but it will be possible with other configurations rather than the ones simulated in this work.
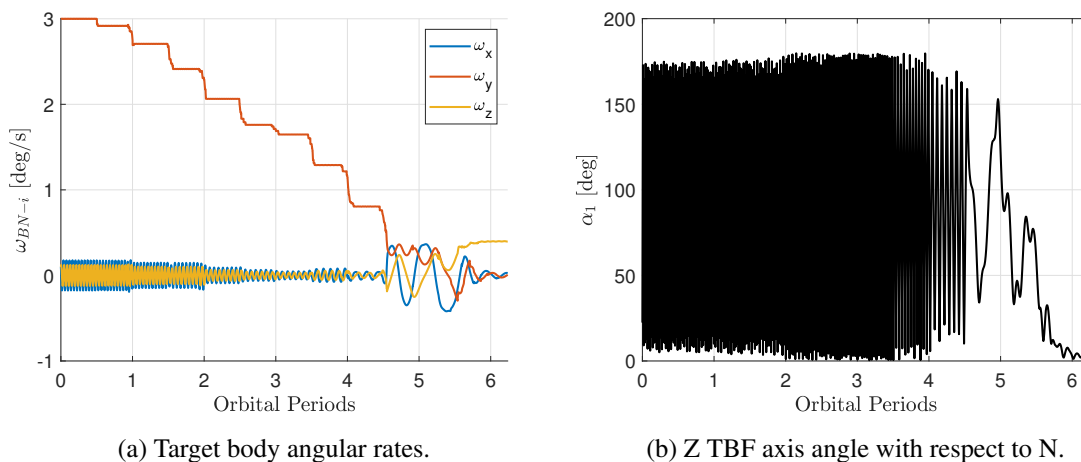


(a) Target body angular rates.

(b) Z TBF axis angle with respect to N.

**Figure 9**: Results for single simulation of the scenario 3 spin redirection control to target 1 with initial condition $\omega_0 = [0.1, 3, 0.1]$ deg/s.

In contrast, the control to the minor body spin without acting its redirection of the spin minor spin axis shows a much better behavior in the simulations. Figure 10 shows the angular rates in the TBF of two representative simulations of target 1 (left) and target 2 (right).

The overall results for scenario 3 in terms of effectiveness and cost are reported in Table 7, where only the body spin control considered effective is reported in terms of mean and standard deviation of the impingement thruster propellant cost, while the N redirection spin are marked ineffective with an X mark. The body spin control of scenario 3 presents costs in terms of propellant that are comparable with the body spin control of scenario 2. In some cases, i.e. with the tumbling initial condition, the minor inertia axis spin generation in the TBF is less expensive with respect to the major inertia axis spin generation. In fact, due the already discussed limited control authority to obtain the torques along the minor axis direction, the scenario 3 benefits from the fact that residual angular momentum is left exactly along the axis where the impingement control has less capability in acting. The cost of scenario 3 with respect to scenario 2 is also less in the case where the initial target angular velocity is along the minor axis of the TBF. In this case, scenario 2 has to generate the angular rate along the minor axis from a different condition while in scenario 3, the initial angular
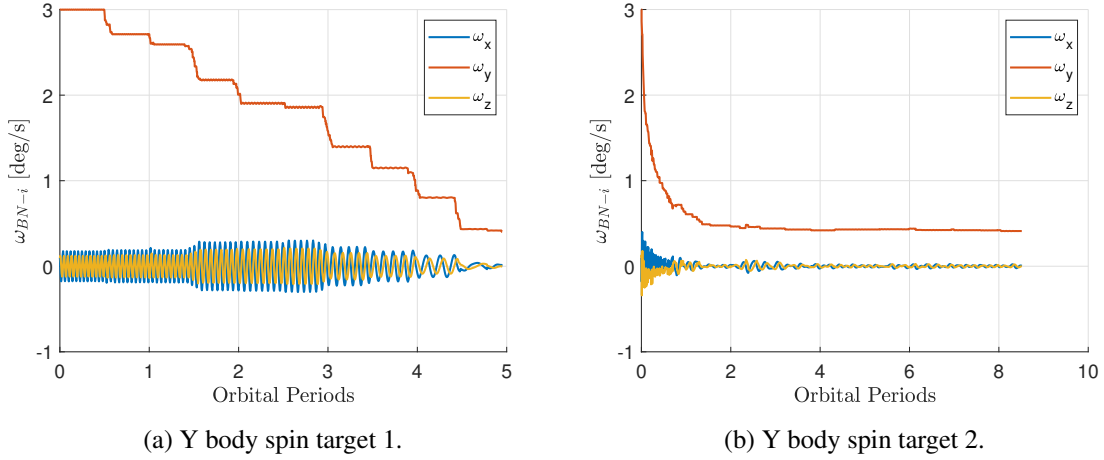
16

(a) Y body spin target 1.



(b) Y body spin target 2.

**Figure 10**: Results for single simulation of the scenario 3 body spin control with initial condition $\omega_0 = [0.1, 3, 0.1]$ deg/s for the two different targets.

momentum is already along the minor axis so it is just damped to the desired rate. As for the previous results, some simulations of target 2 are not successful, for the reasons already discussed in previous results.

**Table 7**: Simulations results for scenario 3.

|  |  | $\overline{m}_p$ [kg] | | $\sigma_{mp}$ [kg] | | $\max(m_p)$ [kg] | |
|---|---|---|---|---|---|---|---|
|  | $\omega_0$ [deg/s] | S/C 1 ($N_f$) | S/C 2 ($N_f$) | S/C 1 | S/C 2 | S/C 1 | S/C 2 |
| RTN Spin | $[\sqrt{3}, \sqrt{3}, \sqrt{3}]$ | ✗ | ✗ | ✗ | ✗ | ✗ | ✗ |
|  | $[3, 0.1, 0.1]$ | ✗ | ✗ | ✗ | ✗ | ✗ | ✗ |
|  | $[0.1, 3, 0.1]$ | ✗ | ✗ | ✗ | ✗ | ✗ | ✗ |
|  | $[0.1, 0.1, 3]$ | ✗ | ✗ | ✗ | ✗ | ✗ | ✗ |
| Body spin | $[\sqrt{3}, \sqrt{3}, \sqrt{3}]$ | 0.358 | 0.303 (1) | 0.069 | 0.206 | 0.548 | 1.443 |
|  | $[3, 0.1, 0.1]$ | 0.310 | 0.343 (2) | 0.080 | 0.170 | 0.717 | 1.280 |
|  | $[0.1, 3, 0.1]$ | 1.262 | 0.562 | 0.092 | 0.162 | 1.561 | 1.029 |
|  | $[0.1, 0.1, 3]$ | 1.523 | 0.496 | 0.198 | 0.167 | 1.992 | 1.241 |

**Result discussion**

In light of the simulations results, the impingement control is feasible to obtain most of the stable attitude motions to increase the collaborativeness of the target. The actual selection of the optimal scenario to be applied during the in orbit operations prior to capture of an uncontrolled satellite is highly dependent on the initial angular velocity of the target, and its geometry and inertia characteristics. In fact, it is seen from this study that target 1, that shows more symmetrical properties and configuration of its surfaces with respect to the center of mass, is characterized by an higher robustness in achieving the control objective with impingement. Whereas, the target 2 proved to

be harder to be controlled and more dependent on the initial motion and facing of its surfaces with respect to the chaser. This behavior can be slightly corrected, considering as candidates points $N_t$ for the pointing of the thruster in the impingement algorithm only the ones on the cubic satellite body. However, the torques obtained firing on the panel have the capability of being much higher in magnitude, thanks to the higher distance of the force application with respect to the center of mass. Therefore, aiming also at the panel, less firing can be used to achieve the same objective, thus propellant cost is greatly lowered.

Referring to both the possible safe approach directions in the different scenarios, and the impingement control performances of each scenario, the positions along the major inertia body axis can be identified as an advantageous locations of the grapple fixture targeted by the chaser manipulator. In fact, the impingement control is extremely reliable in obtaining either a full detumbling or the major axis spin, with comparable cost. The location along the minor axis of inertia can still be managed in the scenarios. In particular, considering a translational synchronization in scenario 2 and a rotational synchronization in scenario 3, contrarily to the conditions defined previously. In this cases the grapple fixture will be placed in locations where large appendages are, so it may be less feasible in terms of space available in the target platform. However, for the target 2, assumed as the debris example in the paper, placing the grapple fixture in the -Y face opposite to the panel can be a viable solution from the manipulator safe operations point of view. Instead, the placing of the grapple fixture on the surfaces with normal vectors parallel to the intermediate inertia axis will raise problems in particular in scenario 2, where that location is span by the large appendages of the target. In scenario 1 and 3, the operations can still be manageable, in particular in scenario 3, where only the phasing of the synchronized motion around the target can be adjusted to approach the X face instead of the Z face.

**CONCLUSIONS**

In this paper, the contactless control of the tumbling state of an uncooperative and non collaborative failed small satellite is treated. The target failed satellite has been controlled, with the plume impingement strategy, to stable end conditions which can greatly aid the autonomous and safe final approach and capture operations. The impingement performances to achieve a detumbling control are the most robust among the analyzed set. However, some particular spin control cases can result in propellant saving, still increasing the collaboration of the target spacecraft. For this cases, the location of the grapple fixture is of great importance in order to define the feasibility. It is discussed, that, according to both the robustness and cost of the impingement control in different control scenarios, if the grapple fixture is located along the major axis (e.g. the $\pm$ faces in the targets considered in this paper), the control scenarios are all viable in terms of safe capture operations. So in this case, the guidance to be applied can be chosen according to advantageous solutions dependent on the initial conditions. Future work and developments will comprehend a refinement of the impingement operations simulation model including also station keeping and chaser attitude control, in order to better estimate the cost of the operations and its dependency with the system geometry parameters, i.e. chaser target separation. In addition, other spacecraft geometry and sizes will be analyzed, together with different guidance laws, and sensitivity to the main parameters of the systems will be performed, being the real system properties in general intrinsically uncertain.

## ACKNOWLEDGMENT

## REFERENCES

[1] C. Bonnal, J.-M. Ruault, and M.-C. Desjean, "Active debris removal: Recent progress and current trends," *Acta Astronautica*, Vol. 85, 2013, pp. 51 – 60, https://doi.org/10.1016/j.actaastro.2012.11.009.

[2] J.-C. Liou, N. Johnson, and N. Hill, "Controlling the growth of future LEO debris populations with active debris removal," *Acta Astronautica*, Vol. 66, No. 5, 2010, pp. 648 – 653, https://doi.org/10.1016/j.actaastro.2009.08.005.

[3] J. Liou, "Active debris removal and the challenges for environment remediation," 2012.

[4] J. L. Forshaw, G. S. Aglietti, S. Fellowes, T. Salmon, I. Retat, A. Hall, T. Chabot, A. Pisseloup, D. Tye, C. Bernal, F. Chaumette, A. Pollini, and W. H. Steyn, "The active space debris removal mission RemoveDebris. Part 1: From concept to launch," *Acta Astronautica*, Vol. 168, 2020, pp. 293 – 309, https://doi.org/10.1016/j.actaastro.2019.09.002.

[5] R. Biesbroek, L. Innocenti, A. Wolahan, and S. M. Serrano, "e. Deorbit–ESA's Active Debris Removal Mission," *Proceedings of the 7th European Conference on Space Debris*, ESA Space Debris Office, 2017, p. 10.

[6] "ClearSpace," `https://clearspace.today/`. Accessed: 2020-06-28.

[7] S. Efimov, D. Pritykin, and V. Sidorenko, "Defunct Satellites in Nearly Polar Orbits: Long-term Evolution of Attitude Motion," *Baltic astronomy an international journal*, Vol. 27, 11 2018, pp. 264–277, 10.1515/Astro-2018-0029.

[8] L. B. M. Sagnières and I. Sharf, "Long-Term Rotational Motion Analysis and Comparison to Observations of the Inoperative Envisat," *Journal of Guidance, Control, and Dynamics*, Vol. 42, No. 2, 2019, pp. 364–376, 10.2514/1.G003647.

[9] B. B. Virgili, S. Lemmens, and H. Krag, "Investigation on Envisat attitude motion," *e. Deorbit workshop*, 2014.

[10] R. Lampariello, "On Grasping a Tumbling Debris Object with a Free-Flying Robot," *IFAC Proceedings Volumes*, Vol. 46, No. 19, 2013, pp. 161 – 166. 19th IFAC Symposium on Automatic Control in Aerospace, https://doi.org/10.3182/20130902-5-DE-2040.00118.

[11] C. Ma, C. Wei, and J. Yuan, "Semisynchronizing Strategy for Capturing a High-Speed Tumbling Target," *Journal of Guidance, Control, and Dynamics*, Vol. 41, No. 12, 2018, pp. 2615–2632, 10.2514/1.G003459.

[12] J. Ventura, M. Ciarcià, M. Romano, and U. Walter, "Fast and Near-Optimal Guidance for Docking to Uncontrolled Spacecraft," *Journal of Guidance, Control, and Dynamics*, Vol. 40, No. 12, 2017, pp. 3138–3154, 10.2514/1.G001843.

[13] S. Corpino, S. Mauro, S. Pastorelli, F. Stesina, G. Biondi, L. Franchi, and T. Mohtar, "Control of a Noncooperative Approach Maneuver Based on Debris Dynamics Feedback," *Journal of Guidance, Control, and Dynamics*, Vol. 41, 10 2017, pp. 1–18, 10.2514/1.G002685.

[14] L. Breger and J. P. How, "Safe Trajectories for Autonomous Rendezvous of Spacecraft," *Journal of Guidance, Control, and Dynamics*, Vol. 31, No. 5, 2008, pp. 1478–1489, 10.2514/1.29590.

[15] J. Ge, J. Zhao, and J. Yuan, "A novel guidance strategy for autonomously approaching a tumbling target," *Proceedings of the Institution of Mechanical Engineers, Part G: Journal of Aerospace Engineering*, Vol. 232, 03 2017, p. 095441001769900, 10.1177/0954410017699006.

[16] Q. Li, J. Yuan, B. Zhang, and H. Wang, "Artificial potential field based robust adaptive control for spacecraft rendezvous and docking under motion constraint," *ISA Transactions*, Vol. 95, 2019, pp. 173 – 184, https://doi.org/10.1016/j.isatra.2019.05.018.

[17] M. Kaplan, B. Boone, R. Brown, T. Criss, and E. Tunstel, "Engineering Issues for All Major Modes of In Situ Space Debris Capture," 08 2010, 10.2514/6.2010-8863.

[18] R. Delage, *An Overview of ATV Integrated Mission Analysis and Mission Preparation*, 10.2514/6.IAC-03-V.2.09.

[19] H. B. Hablani, M. L. Tapper, and D. J. Dana-Bashian, "Guidance and Relative Navigation for Autonomous Rendezvous in a Circular Orbit," *Journal of Guidance, Control, and Dynamics*, Vol. 25, No. 3, 2002, pp. 553–562, 10.2514/2.4916.

[20] Y. Ariba, D. Arzelier, L. S. Urbina, and C. Louembet, "V-bar and R-bar Glideslope Guidance Algorithms for Fixed-Time Rendezvous: A Linear Programming Approach," *20th IFAC Symposium on Automatic Control in Aerospace*, Sherbrooke, Canada, Aug. 2016.

[21] Y.-Q. Liu, Z.-W. Yu, X.-F. Liu, and G.-P. Cai, "Active detumbling technology for high dynamic noncooperative space targets," *Multibody System Dynamics*, Vol. 47, Sep 2019, pp. 21–41, 10.1007/s11044-019-09675-3.

[22] W. Cheng, Z. Li, and Y. He, "Strategy and Control for Robotic Detumbling of Space Debris by Using Flexible Brush," *2019 3rd International Conference on Robotics and Automation Sciences (ICRAS)*, 2019, pp. 41–47.

[23] T. Bennett, D. Stevenson, E. Hogan, and H. Schaub, "Prospects and challenges of touchless electrostatic detumbling of small bodies," *Advances in Space Research*, Vol. 56, No. 3, 2015, pp. 557 – 568. Advances in Asteroid and Space Debris Science and Technology - Part 1, https://doi.org/10.1016/j.asr.2015.03.037.

[24] N. Ortiz, S. Walker, M. Jankovic, J. M. Romero Martin, F. Kirchner, and M. Vasile, "Control analysis for a contactless de-tumbling method based on eddy currents: problem definition and approximate proposed solutions," 01 2016, 10.2514/6.2016-0642.

[25] R. Kumar and R. J. Sedwick, "Despinning Orbital Debris Before Docking Using Laser Ablation," *Journal of Spacecraft and Rockets*, Vol. 52, No. 4, 2015, pp. 1129–1134, 10.2514/1.A33183.

[26] M. Vetrisano, N. Thiry, and M. Vasile, "Detumbling large space debris via laser ablation," *IEEE Aerospace Conference Proceedings*, Vol. 2015, 06 2015, 10.1109/AERO.2015.7119051.

[27] Y. Nakajima, H. Tani, T. Yamamoto, N. Murakami, S. Mitani, and K. Yamanaka, "Contactless Space Debris Detumbling: A Database Approach Based on Computational Fluid Dynamics," *Journal of Guidance, Control, and Dynamics*, Vol. 41, No. 9, 2018, pp. 1906–1918, 10.2514/1.G003451.

[28] Y. Nakajima, S. Mitani, H. Tani, N. Murakami, T. Yamamoto, and K. Yamanaka, *Detumbling Space Debris via Thruster Plume Impingement*, 10.2514/6.2016-5660.

[29] T. V. Peters and D. Escorial Olmos, "COBRA contactless detumbling," *CEAS Space Journal*, Vol. 8, Sep 2016, pp. 143–165, 10.1007/s12567-016-0116-6.

[30] F. Ferrari, R. Benvenuto, and M. Lavagna, "GAS PLUME IMPINGEMENT TECHNIQUE FOR SPACE DEBRIS DE-TUMBLING," 06 2014.

[31] W. Fehse, *Automated Rendezvous and Docking of Spacecraft*. Cambridge Aerospace Series, Cambridge University Press, 2003, 10.1017/CBO9780511543388.

[32] I. D. Boyd, *Modelling of satellite control thruster plumes*. PhD thesis, University of Southampton, October 1988.

[33] F. L. Markley and J. L. Crassidis, *Fundamentals of spacecraft attitude determination and control*, Vol. 33. Springer, 2014.